LETTER

doi:10.1038/nature14090

Effects of electron correlations on transport properties of iron at Earth's core conditions

Peng Zhang[1], R. E. Cohen[1,2] & K. Haule[3]

Earth's magnetic field has been thought to arise from thermal convection of molten iron alloy in the outer core, but recent density functional theory calculations have suggested that the conductivity of iron is too high to support thermal convection[1–4], resulting in the investigation of chemically driven convection[5,6]. These calculations for resistivity were based on electron–phonon scattering. Here we apply self-consistent density functional theory plus dynamical mean-field theory (DFT + DMFT)[7] to iron and find that at high temperatures electron–electron scattering is comparable to the electron–phonon scattering, bringing theory into agreement with experiments and solving the transport problem in Earth's core. The conventional thermal dynamo picture is safe. We find that electron–electron scattering of *d* electrons is important at high temperatures in transition metals, in contrast to textbook analyses since Mott[8,9], and that 4*s* electron contributions to transport are negligible, in contrast to numerous models used for over fifty years. The DFT+DMFT method should be applicable to other high-temperature systems where electron correlations are important.

Recent DFT calculations by Pozzo *et al.*[3] predict the electrical resistivity of iron to be (6.3–7.5) $\times 10^{-5}\,\Omega$ cm at temperatures from 4,580 K to 6,400 K and pressures from 120 GPa to 340 GPa. The thermal conductivities they predicted are approximately three times the currently used values of 46–63 W m^{-1} K^{-1} in geophysics[10]. The results of Pozzo *et al.*[3] are consistent with previous DFT studies[1,2,4,11]. The large electrical and thermal conductivities, however, challenge current Earth models.

Efforts to constrain the transport properties of iron at core conditions have a long history. Elsasser estimated the resistivity of iron to be $\rho \approx 10.0 \times 10^{-5}\,\Omega$ cm at core conditions on the basis of geophysical arguments[12]. By assuming the resistivity of iron to be constant along the melting line, Stacey and Anderson obtained $\rho = 11.2 \times 10^{-5}\,\Omega$ cm at 4,971 K and 330 GPa (ref. 10).

All previous calculations neglect electron–electron scattering. It has long been believed that resistivity in ordinary metals arises primarily from electron–phonon scattering, except at cryogenic conditions[9]. Calculations of resistivity from electron–electron scattering only now have become possible owing to developments in computational theory and technology and access to large-scale computational resources. The DFT + DMFT approach has proved successful in providing results that are in good agreement with experiments for iron-bearing compounds[13,14] and other strongly correlated materials. It quantitatively predicts properties such as magnetic moments and the effective mass of a series of compounds in iron pnictides and iron chalcogenides. It also explains why superconducting gaps in these compounds are strongly Fermi-surface dependent.

Our primary interest is in the properties of Earth's core, so we first present resistivities at the core density of iron (throughout we refer to Earth's core density from seismology of 13.04 g cm^{-3}, or an atomic volume of 47.8 atomic units = 7.083 Å^3) (Fig. 1). The resistivities calculated by Sha and Cohen[1], de Koker *et al.*[2] and Pozzo *et al.*[3] at the core conditions are approximately half the value obtained by extrapolating from the systematics of Stacey and Anderson[10] and half the value obtained by extrapolating from previous shock compression experimental results[15–17]. The thermal conductivity k of pure iron at core conditions obtained from their[3] calculations ranges from 150 W m^{-1} K^{-1} to about 250 W m^{-1} K^{-1}. Assuming a large thermal conductivity, the calculated heat conduction down the core adiabat is about 15 terawatts (TW)[3], which overlaps the estimates[18,19] of total heat loss from the core of 8–16 TW. No energy is left to drive the thermal convection in the geodynamo. To sustain the geodynamo, compositional convection is therefore required[3,5]. However, this mechanism leads to a new paradox:[6] Earth's inner core solidification is believed to have started about one billion years ago[4], so before that there would be no compositional convection to drive the dynamo, yet we know that Earth's geodynamo has existed for more than 3.4 billion years[20].

We find that at high temperatures the resistivity from electron–electron scattering, ρ_{ee}, computed with DFT + DMFT is of the same order as the electron–phonon scattering, ρ_{ep}, computed with DFT (Fig. 1)[1]. The sum of the two parts of the resistivity, from the electron–electron and the electron–phonon scattering, is in agreement with earlier geophysical estimates. After including both the electron–electron scattering and the electron–phonon scattering, traditional resistivity values are recovered. We checked the systematics of Stacey and Anderson using resistivity results at other density as well. Considering the uncertainty of iron's melting temperature ($\sim \pm 500$ K) the resistivity of iron is around $13.5 \times 10^{-5}\,\Omega$ cm along its melting line. Our results support Stacey and Anderson's systematics.

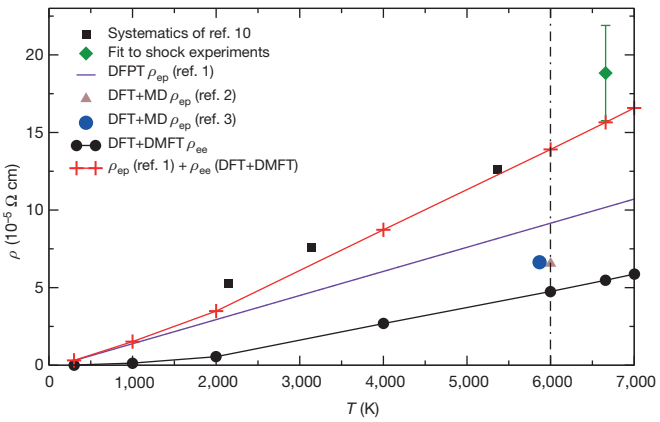

Figure 1 | Resistivity versus temperature of hcp iron at Earth's core density. The black vertical line indicates Earth's core temperature[30,31]. The black squares are the extrapolations to this density using the systematics of Stacey and Anderson[10]. The green diamond is an interpolation to this density of previous shock compression results[15–17]. The DFPT resistivity line is from the linear extrapolation of low-temperature results[1,32]. The DFT + molecular dynamics (MD) resistivities are extracted from refs 2,3. The statistical error bars of DFT + DMFT and the total resistivities are smaller than their symbols. Values are given in the Extended Data Tables 1 and 2. All error bars are 1σ.

[1]Geophysical Laboratory, Carnegie Institution of Washington, 5251 Broad Branch Road NW, Washington DC 20015, USA. [2]Department of Earth Sciences, University College London, 222 Pearson Building, Gower Street, London WC1E 6BT, UK. [3]Department of Physics, Rutgers University, Piscataway, New Jersey 08854, USA.

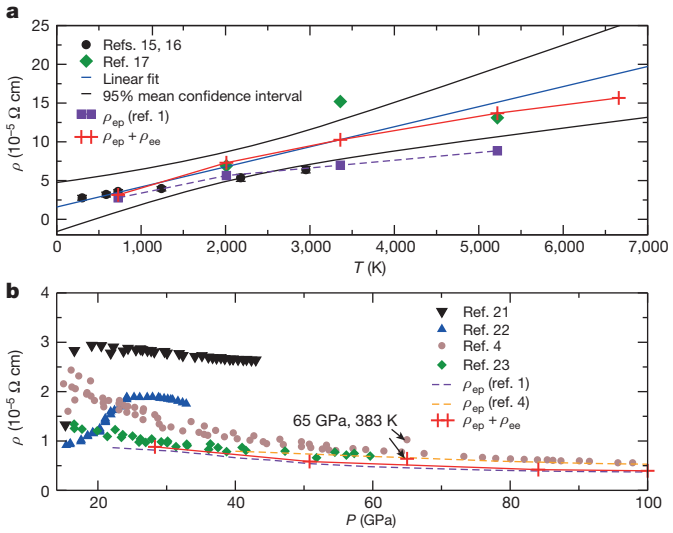

Figure 2 | Our computed resistivities of hcp iron are compared with experimental results. **a**, Resistivity versus temperature along the Hugoniot from shock data[15–17], electron–phonon scattering from DFPT calculations[1] (violet), and electron–phonon scattering (DFPT) plus electron–electron scattering (DFT + DMFT) (red). The blue line is the linear fit of shock compression data, and the black lines are the 95% mean confidence interval. **b**, Resistivity versus pressure at $T = 300$ K and at $P = 65$ GPa, $T = 383$ K. Previous diamond anvil cell experimental results[4,21–23] are compared with the DFPT calculations of ref. 1 (violet dashed lines) and ref. 4 (orange dashed lines). The data of refs 21,22 were analysed in ref. 1. Red plus symbols indicate the sum of DFPT electron–phonon[1] and our DFT + DMFT electron–electron resistivities. The statistical 1σ error bars of total resistivities are smaller than their symbols. Values are given in Extended Data Tables 1 and 2.

Direct comparisons of our results with shock compression and diamond anvil cell experimental resistivities are provided in Fig. 2. Along the Hugoniot, we find that our electron–phonon plus electron–electron resistivities are linear at high temperatures (Fig. 2a). So we fitted the shock data along the Hugoniot to a straight line as well, and also derived the 95% mean confidence interval from the data. It is not justified to fit a higher-order function to the data given the experimental scatter. The total resistivity $\rho_{ep} + \rho_{ee}$, which is the summation of the density functional perturbation theory (DFPT) and DFT + DMFT results, nicely overlaps the best-fitting line of the shock data. In contrast, the ρ_{ep} line falls below the confidence interval, showing that it is a poor model to explain the results. We note that Keeler *et al.*'s[15,16] error bars are too small, both from the scatter of their own data, and from Bi *et al.*[17], which provided no error estimates. Furthermore, Bi *et al.* suggested that Keeler *et al.*'s values were systematically low, owing to shunting of the current. Our total resistivities $\rho_{ee} + \rho_{ep}$ agree well within experimental error with diamond anvil cell experimental results at room temperature[4,21–23], and also at the $P = 65$ GPa, $T = 383$ K point of ref. 4. Our results are in slightly better agreement with Seagle *et al.*[23] than with Gomi *et al.*[4], but this difference probably represents the experimental uncertainty, since both are state-of-the-art experiments. At room temperature the resistivity from the electron–electron scattering is insignificant relative to that from the electron–phonon scattering. We expect resistivity contributions also from defects and grain boundaries, and the DFT electron–phonon values do not include contributions from antiferromagnetic correlations[24,25], which are expected to be important at moderate to low temperatures. We find that the temperature dependence of the resistivity is much more important than changes with pressure.

When the mean-free path is comparable to the lattice spacings, saturation in resistivity is expected at the Ioffe–Regel value for the electron–phonon component. We estimate the saturation resistivity to be $11.4 \times 10^{-5}\,\Omega$ cm at the core density, which is higher than our estimated resistivity for electron–phonon scattering at $\rho_{ep} = 9.15 \times 10^{-5}\,\Omega$ cm at 6,000 K. Since the resistivity from electron–electron scattering may exceed the Ioffe–Regel value[26], we do not expect saturation effects to be important at the core conditions.

We estimate the thermal conductivity using the Wiedemann–Franz law ($k = LT/\rho$, with Lorentz parameter $L = 2.44 \times 10^{-8}\,\mathrm{W\,\Omega\,K^{-2}}$), giving about 105 $\mathrm{W\,m^{-1}\,K^{-1}}$ at temperatures from 4,000 K to 7,000 K. Earth's core is not pure crystalline iron but is liquid and contains light elements of the order of 10% by mass. Since the light elements will decrease the electrical and thermal conductivities, this thermal conductivity is close to previously accepted values[10]. Furthermore, resistivity increases with melting[27], so that there is now no problem driving the dynamo with thermal convection. Although the absolute values of the core resistivity and thermal conductivity cannot be constrained exactly owing to uncertainties in temperature and composition, it is clear (1) that electron–electron scattering is an important component, and (2) that including electron–electron scattering removes any problem with core conductivity being too high to explain the geodynamo. Thus, the transport crisis is solved.

Contrary to general belief that at high temperatures the resistivity of transition metals comes mainly from electron–phonon scattering[9], our DFT + DMFT computations have shown that the electron–electron scattering is as important as the electron–phonon scattering in hexagonal close packed (hcp) iron. According to the Fermi-liquid theory, at low temperature T the resistivity of metals from electron–electron scattering $\rho_{ee}(T)$ is proportional to T^2. Mott suggested that the T^2 behaviour would have a broad crossover region before saturating, but gave no theory for the form, nor has one yet been developed[8]. Above 2,000 K, we find $\rho_{ee}(T)$ in Fig. 1 to be linear with temperature at constant volume. Interestingly, the linear T dependence of resistivity is widely observed in correlated materials, including high-temperature superconducting cuprates[28], heavy Fermion and other correlated metals[26,29]. In DMFT simulations of the Hubbard model[26,29], linear-T resistivity arises from the linear-T dependence of quasiparticle weight at temperatures above the Fermi-liquid coherent energy scale. However, in hcp iron we find that the quasiparticle weight is only weakly dependent on temperature. As shown in Fig. 3a, the conduction electron scattering rate Γ is linear with T above 2,000 K.

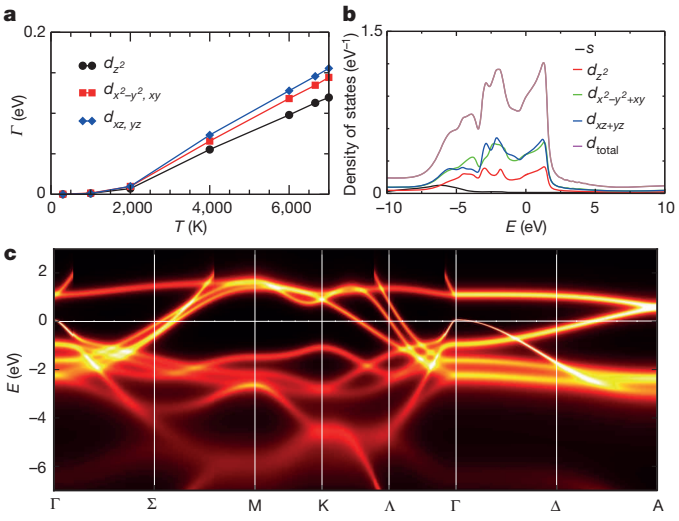

Figure 3 | Scattering rates, density of states and spectral function at Earth's core density of hcp iron. **a**, Orbitally resolved scattering rates as a function of temperature. $\Gamma_{d_{z^2}}$, $\Gamma_{d_{x^2-y^2,xy}}$ and $\Gamma_{d_{xz,yz}}$ represent the scattering rates on respective d orbitals. **b**, Density of states of s, d_{z^2}, $d_{x^2-y^2+xy}$, d_{xz+yz} and d_{total} orbitals at 6,000 K. **c**, Spectral function $A(k, E)$, where k is the wave vector and E is the electron energy relative to the Fermi level, at 6,000 K. The x axis is the k-path in the first Brillouin zone of the hcp lattice. The statistical 1σ error bars of the scattering rates are smaller than their symbols.

Since the density of *s* electrons at the Fermi level, $N_s(E_F)$, is very small (Fig. 3b) and in our calculations $N_s(E_F)/[N_s(E_F) + N_d(E_F)] < 1\%$ (where E_F is the Fermi energy and $N_{s,d}$ is the partial density of states) at all temperatures, $\rho_{ee}(T)$ is determined mostly by the scattering rates of *d*-electrons in hcp iron. We suggest that the linear-T scattering in iron arises from scattering off thermally excited local states which originate from strong electron–electron interactions, a process not included in Fermi-liquid theory. In contrast, the linear resistivity from electron–phonon scattering comes from the near-linear dependence on number of phonons (the quantized lattice vibrations) with temperature.

We find correlated bands in the low-energy region, all being iron 3*d* states (Fig. 3b, 3c). The correlated states at the Fermi level are the origin of large electron–electron scattering and substantial electron–electron resistivity. We expect some other transition metals to have incoherent states at E_F and to show similar behaviour, and those with sharp quasi-particle states at E_F to have normal behaviour with dominant electron–phonon resistivity.

Online Content Methods, along with any additional Extended Data display items and Source Data, are available in the online version of the paper; references unique to these sections appear only in the online paper.

Received 6 April; accepted 11 November 2014.

1. Sha, X. & Cohen, R. E. First-principles studies of electrical resistivity of iron under pressure. *J. Phys. Condens. Matter* **23,** 075401 (2011).
2. de Koker, N., Steinle-Neumann, G. & Vlček, V. Electrical resistivity and thermal conductivity of liquid Fe alloys at high P and T, and heat flux in Earth's core. *Proc. Natl Acad. Sci. USA* **109,** 4070–4073 (2012).
3. Pozzo, M., Davies, C., Gubbins, D. & Alfè, D. Thermal and electrical conductivity of iron at Earth's core conditions. *Nature* **485,** 355–358 (2012).
4. Gomi, H. *et al.* The high conductivity of iron and thermal evolution of the Earth's core. *Phys. Earth Planet. Inter.* **224,** 88–103 (2013).
5. Buffett, B. Geomagnetism under scrutiny. *Nature* **485,** 319–320 (2012).
6. Olson, P. The new core paradox. *Science* **342,** 431–432 (2013).
7. Haule, K., Yee, C. & Kim, K. Dynamical mean-field theory within the full-potential methods: electronic structure of $CeIrIn_5$, $CeCoIn_5$, and $CeRhIn_5$. *Phys. Rev. B* **81,** 195107 (2010).
8. Mott, N. F. Electrons in transition metals. *Adv. Phys.* **13,** 325–422 (1964).
9. Allen, P. B. Electron transport. *Contemp. Concepts Condens. Matter Sci.* **2,** 165–218 (2006).
10. Stacey, F. D. & Anderson, O. L. Electrical and thermal conductivities of Fe-Ni-Si alloy under core conditions. *Phys. Earth Planet. Inter.* **124,** 153–162 (2001).
11. Pozzo, M., Davies, C., Gubbins, D. & Alfè, D. Thermal and electrical conductivity of solid iron and iron-silicon mixtures at Earth's core conditions. *Earth Planet. Sci. Lett.* **393,** 159–164 (2014).
12. Elsasser, W. M. Induction effects in terrestrial magnetism. Part II. The secular variation. *Phys. Rev.* **70,** 202–212 (1946).
13. Yin, Z. P., Haule, K. & Kotliar, G. Kinetic frustration and the nature of the magnetic and paramagnetic states in iron pnictides and iron chalcogenides. *Nature Mater.* **10,** 932–935 (2011).
14. Mandal, S., Cohen, R. E. & Haule, K. Strong pressure dependent electron-phonon coupling in FeSe. *Phys. Rev. B* **89,** 220502 (2014).
15. Keeler, R. N. & Mitchell, A. C. Electrical conductivity, demagnetization, and the high-pressure phase transition in shock-compressed iron. *Solid State Commun.* **7,** 271–274 (1969).
16. Keeler, R. N. & Royce, E. B. in *Physics of High Energy Density* (eds Caldirola, P. & Knoepfel, H.) 106–125 (Proceedings of the International School of Physics Enrico Fermi Vol. 48, 1971).
17. Bi, Y., Tan, H. & Jing, F. Electrical conductivity of iron under shock compression up to 200 GPa. *J. Phys. Condens. Matter* **14,** 10849–10854 (2002).
18. Lay, T., Hernlund, J. & Buffett, B. A. Core-mantle boundary heat flow. *Nature Geosci.* **1,** 25–32 (2008).
19. Wu, B., Driscoll, P. & Olson, P. A statistical boundary layer model for the mantle *D″* region. *J. Geophys. Res.* **116,** B12112 (2011).
20. Tarduno, J. A. *et al.* Geodynamo, solar wind, and magnetopause 3.4 to 3.45 billion years ago. *Science* **327,** 1238–1240 (2010).
21. Balchan, A. S. & Drickamer, H. G. High pressure electrical resistance cell, and calibration points above 100 kilobars. *Rev. Sci. Instrum.* **32,** 308, http://dx.doi.org/10.1063/1.1717350 (1961).
22. Reichlin, R. L. Measuring the electrical resistance of metals to 40 GPa in the diamond-anvil cell. *Rev. Sci. Instrum.* **54,** 1674, http://dx.doi.org/10.1063/1.1137308 (1983).
23. Seagle, C. T., Cottrell, E., Fei, Y., Hummer, D. R. & Prakapenka, V. B. Electrical and thermal transport properties of iron and iron-silicon alloy at high pressure. *Geophys. Res. Lett.* **40,** 5377–5381 (2013).
24. Steinle-Neumann, G., Cohen, R. E. & Stixrude, L. Magnetism in iron as a function of pressure. *J. Phys. Condens. Matter* **16,** S1109–S1119 (2004).
25. Steinle-Neumann, G., Stixrude, L. & Cohen, R. E. Magnetism in dense hexagonal iron. *Proc. Natl Acad. Sci. USA* **101,** 33–36 (2004).
26. Deng, X. *et al.* How bad metals turn good: spectroscopic signatures of resilient quasiparticles. *Phys. Rev. Lett.* **110,** 086401 (2013).
27. Deng, L., Seagle, C., Fei, Y. & Shahar, A. High pressure and temperature electrical resistivity of iron and implications for planetary cores. *Geophys. Res. Lett.* **40,** 33–37 (2013).
28. Gurvitch, M. & Fiory, A. T. Resistivity of $La_{1.825}Sr_{0.175}CuO_4$ and $YBa_2Cu_3O_7$ to 1100 K: absence of saturation and its implications. *Phys. Rev. Lett.* **59,** 1337–1340 (1987).
29. Xu, W., Haule, K. & Kotliar, G. Hidden Fermi liquid, scattering rate saturation, and Nernst effect: a dynamical mean-field theory perspective. *Phys. Rev. Lett.* **111,** 036401 (2013).
30. Stixrude, L., Wasserman, E. & Cohen, R. E. Composition and temperature of Earth's inner core. *J. Geophys. Res.* **102,** 24729–24739 (1997).
31. Sha, X. & Cohen, R. E. First-principles thermal equation of state and thermoelasticity of hcp Fe at high pressures. *Phys. Rev. B* **81,** 094105 (2010).
32. Perdew, J. P., Burke, K. & Ernzerhof, M. Generalized gradient approximation made simple. *Phys. Rev. Lett.* **77,** 3865–3868 (1996).

Acknowledgements This work is supported by National Science Foundation (NSF) grants EAR-1214807, DMS-1025392, and DMR-1405303. R.E.C. is supported by the Carnegie Institution and the European Research Council Advanced Grant ToMCaT. K.H. is supported by NSF grant DMR-1405303. This research used the NSF Extreme Science and Engineering Discovery Environment (XSEDE) supercomputer 'Stampede', and also used the resources of the Oak Ridge Leadership Computing Facility at the Oak Ridge National Laboratory, which is supported by the Office of Science of the US Department of Energy under contract number DE-AC05-00OR22725. R.E.C. and P.Z. thank I. Mazin, S. Labrosse and R. Caracas for discussions. We also acknowledge J. Robb for assistance with the manuscript preparation.

Author Contributions R.E.C. designed the project, P.Z. performed the computations, P.Z., R.E.C. and K.H. analysed the results and prepared the paper. The DFT + DMFT code was developed by K.H.

Author Information Reprints and permissions information is available at www.nature.com/reprints. The authors declare no competing financial interests. Readers are welcome to comment on the online version of the paper. Correspondence and requests for materials should be addressed to R.E.C. (rcohen@carnegiescience.edu).

METHODS

Code availability. The DFT + DMFT code was developed by K.H. and is available at http://hauleweb.rutgers.edu/downloads/.

The DFT+DMFT formalism. In the DFT+DMFT method[33,34] a functional (equation 118 of ref. 33) that includes all local two particle irreducible skeleton diagrams is optimized. The interaction Hamiltonian is given by the Slater form (equation 28 of ref. 7) with the Slater integral $F^0 = U$, $F^2 = (14/1.625)\,J$, and $F^4 = (8.75/1.625)\,J$, where U is the Hubbard parameter and J is the Hund's coupling. The double counting energy E_{dc} is calculated from the fully localized limit[35] formula $E_{\mathrm{dc}} = U\left(n^0_{\mathrm{cor}} - \frac{1}{2}\right) - \frac{J}{2}\left(n^0_{\mathrm{cor}} - 1\right)$ and n^0_{cor} is the nominal electron occupancy of the correlated atom (iron in this case). We also tested the around-mean-field double-counting[36] and found an increment of resistivity of up to 16% at core conditions, which is not significant. Our DFT calculations show $n_{\mathrm{cor}} = 6.6$ at the core density of iron, so we choose $n^0_{\mathrm{cor}} = \mathrm{Int}(n_{\mathrm{cor}}) = 7$, where Int means choosing the nearest integer number of n_{cor}. We tested $n^0_{\mathrm{cor}} = 6$ and 8, but did not find large changes, and $n^0_{\mathrm{cor}} = 7$ gives the lowest resistivity. More details are given in ref. 7. In our calculation, we choose an energy window of ± 10 eV around the Fermi level E_{F} for the projector. We use the continuous time quantum Monte Carlo method to sample all diagrams in the hybridization expansion, as described in detail in refs 37 and 38.

The all-electron LAPW (linearized augmented plane wave) WIEN2K code[39] is used for the DFT calculations, with the Wu–Cohen exchange-correlation potential[40]. A test at core conditions with the Perdew–Burke–Ernzerhof exchange-correlation functional did not change the resistivity much (only by 2.5%), indicating that our results are robust. The k-space summation is on a $12 \times 12 \times 12$ grid using a modified tetrahedron integration scheme[41]. The cut-off energy separating the core from valence states is -9.0 Ry. $R_{\mathrm{mt}}K_{\mathrm{max}}$ is 9.0 (where R_{mt} is the smallest atomic sphere radius and K_{max} is the maximum number of wavevectors used) and the magnitude of the largest vector GMAX is 19.0. There is no spin-orbital coupling/splitting in our calculation.

The DFT+DMFT method iterates as follows: (1) the lattice problem is solved as in DFT, but with added self-energy for the correlated states (which is zero for the first iteration), which makes the problem non-Hermitian and frequency dependent. The eigenvalues, wavefunctions, charge density and potential are output. Step 1 can be iterated as an inner loop. (2) The impurity levels E_{imp} and the hybridization function $\Delta(\omega)$ between the lattice and the impurity are computed and input into the continuous time quantum Monte Carlo impurity solver to find the DMFT solution. Step 2 can be iterated as an inner loop. (3) The self-energy and the electron density are updated; the new self-energy and electron density are inserted into step (1) and (2) for the next DFT+DMFT iteration.

For Earth's core density of hcp iron we use 13.04 g cm^{-3} and the corresponding lattice volume of 47.8 atomic units[42,43]. The pressure–temperature relationship at this density is presented in Extended Data Fig. 1. The lattice parameter ratio c/a is 1.615 at all volumes[44]. We used a Hubbard $U = 5$ eV and Hund's coupling $J = 0.943$ eV on the basis of numerous previous studies of iron compounds. We checked that $U = 2$ eV gives very similar results; the resistivity is weakly dependent on U (the largest difference is smaller than 12%). Reducing J to zero halves the computed electron–electron resistivity, showing that the Hund's coupling is quantitatively important but not solely responsible for the scattering. Reducing U and J to near zero reduces the electronic resistivity to near zero, as expected. Without the electron–electron correlations, the electron–phonon interactions would dominate, as previously believed.

Accuracy of the DFT + DMFT method. The DFT + DMFT method combines the accurate treatment of the many-body physics as well as a fully self-consistent treatment of the crystal and atomic bonding and hybridization. The DFT + DMFT method is one of the most important advances in numerical simulation of condensed matter physics. By introducing correlation effects, this method works in the region where DFT fails to predict experimental results. Its accuracy has been proved in research on various correlated electron materials from transition metals and their compounds to heavy fermion materials[33,45]. At ambient conditions the transition-metal oxide FeO is an insulator but DFT predicts it to be a metal[46]. In contrast, DFT + DMFT not only makes FeO an insulator at ambient conditions, but also successfully predicted the existence of a metallic phase at high pressure[47]. DFT + DMFT has also been used in research on heavy fermion materials. Using DFT + DMFT, Shim *et al.*[48] identified the ground-state electronic configurations of curium and plutonium. They found that curium has a single-valence ground state with magnetic ordering, whereas plutonium has a ground state that comes from superposition of two atomic valences. The different magnetic properties of curium and plutonium are explained by the interplay between their ground-state electronic configurations, the electronic itinerancy and localization, as well as the spin-orbit coupling. The same group also investigated $CeIrIn_5$ using DFT + DMFT[49], where they found the numerically calculated temperature resolved spectral functions to be in good agreement with experimental results. The consistency between numerical simulations and experimental results enabled them to explain the experimentally observed features in the optical conductivity. The accuracy of DFT + DMFT predictions are not limited to the single-particle level. In an inelastic neutron scattering experiment of the iron pnictide $BaFe_{1.9}Ni_{0.1}As_2$ by ref. 50, their experimental data were compared with the dynamical magnetic susceptibility from DFT + DMFT calculations. They found systematic consistency between the experimental and the numerical results at different energy and moment slices. From these results, they confirm that magnetic excitations in the iron pnictide $BaFe_{1.9}Ni_{0.1}As_2$ are partially localized, which indicates the strongly correlated nature of this high-temperature superconducting material.

Scattering rate and analytic continuation. In our DFT + DMFT calculations the scattering rate of d electrons at the Fermi level is given by:

$$\Gamma^{\alpha}_{E_{\mathrm{F}}} = -Z^{\alpha}_{\kappa_{\mathrm{F}}}\,\mathrm{Im}\Sigma^{\alpha}(\omega)|_{\omega\to 0} \qquad (2)$$

in which $Z^{\alpha}_{\kappa_{\mathrm{F}}} = [1 - (\partial \mathrm{Re}\Sigma^{\alpha}(\omega)/\partial\omega)]^{-1}|_{\omega\to 0}$, α is the d-orbital index of d_{z^2}, $d_{x^2-y^2,xy}$ and $d_{xz,yz}$ and $\Sigma(\omega)$ is the self-energy in real frequency from maximum entropy (MaxEnt) analytic continuation[51] (Extended Data Figs 2 and 3).

Another DFT + DMFT computation for hcp iron (atomic volume of 47.6 atomic units, hcp lattice ratio $c/a = 1.6$, $U = 3.37$ eV, $J = 0.93$ eV, projection energy window $[-10.8$ eV, 4.0 eV$]$ around the Fermi level, around-mean-field double counting) is presented in ref. 52. We duplicate all of their results by exactly following their methods. In ref. 52 the scattering rate of hcp iron is calculated by extrapolating the imaginary frequency to zero $\Gamma(T, i0^+) = -Z(T, i\omega_n)\mathrm{Im}[\sum(T, i\omega_n)]|_{i\omega_n\to i0^+}$. They claim that hcp iron is in the Fermi-liquid state up to 5,800 K with a quadratic scattering rate in temperature. Although we agree with their results at room temperature, we find very different behaviour at high temperatures. Their extrapolation in imaginary frequency is poorly constrained at high temperatures. At Earth's core temperature ($T = 6{,}000$ K), the first positive imaginary frequency is at $\omega_0 = 1.62$ eV, and there are only two points that could be used in extrapolation below 5 eV. This makes the self-energy, and consequently the scattering rate, at $i0^+$ depend heavily on the choice of extrapolation. In Extended Data Fig. 2, three methods (linear, cubic and Akima) are used to extrapolate the imaginary part of the self-energy to $i0^+$. The results from the three extrapolations are distributed over a wide range. In Extended Data Fig. 2, the imaginary part of self-energy at $i0^+$ ranges from -0.23 eV to -0.12 eV, giving 100% uncertainty for the absolute values. Such uncertainty at high temperatures leads ref. 52 to conclude that hcp iron is a Fermi liquid at high temperatures, which is contrary to our results, owing to insufficient accuracy in their analysis. In contrast, the self-energy from our MaxEnt has a very dense mesh, where the smallest energy scale is 0.0025 eV, as shown in the inset of Extended Data Fig. 3. There is a $\omega = 0$ point, so extrapolation is no longer needed.

Three independent methods were used to check the stability and accuracy of our analytic continuation; we used both the Padé and the singular value decomposition methods in addition to MaxEnt. As presented in Extended Data Fig. 3 and its inset, the imaginary part of the self-energies from the three analytic continuations agree in the low-energy region needed for the conductivity. At energies around the Fermi level, the three analytic continuations give identical self-energies. This proves that our MaxEnt results are precise and stable.

Optical conductivity calculation in DMFT. The optical conductivity is calculated using the self-energy on the real frequency axis from the MaxEnt, with the low frequency limit giving the direct-current conductivity. In DMFT, since the vertex corrections to conductivity can be safely omitted[53], the formula we use in the optical conductivity calculation is[45]

$$\mathrm{Re}\sigma_{\mu,\nu}(\omega) = \pi e^2 \sum_{\mathrm{k}} \int_{-\infty}^{\infty} \mathrm{d}\epsilon \frac{f(\epsilon-\omega) - f(\epsilon)}{\omega} \mathrm{Tr}\left[\rho_{\mathrm{k}}(\epsilon) V^{\mathrm{k},\mu} \rho_{\mathrm{k}}(\epsilon-\omega) V^{\mathrm{k},\nu}\right] \qquad (3)$$

where μ, ν are direction indices, $\rho_{\mathrm{k}}(\epsilon) = \frac{G^{\dagger}_{\mathrm{k}}(\epsilon) - G_{\mathrm{k}}(\epsilon)}{2\pi i}$, the velocity vector $V^{\mathrm{k},\mu}_{i,j} = -\frac{i}{m}\left\langle \psi_{\mathrm{k},i} \middle| \nabla_{\mu} \middle| \psi_{\mathrm{k},j} \right\rangle$ and i, j are orbital indices, the fermionic distribution function $f(\epsilon) = \left(e^{\beta(\epsilon-\mu)} + 1\right)^{-1}$ and the trace is over all valence states.

Equation of state. Our resistivity results at core conditions are independent of any equation of state. We use the known density[43] and the temperature of Earth's core. For our comparisons with experiments under other conditions, we estimate the pressures of our DFT + DMFT calculations from the thermal equation of state given by ref. 31. The Hugoniot line is from the same paper[31]. The pressure–temperature relationship at Earth's core density and along the Hugoniot line are shown in Extended Data Fig. 1.

Extrapolations. In Fig. 1 we estimated the resistivities of iron at Earth's core density using the systematics of ref. 10 as well as three sets of parameters (P, T_{m}) (where T_{m} is the melting temperature of iron) along iron's melting curve[54–56]. Stacey and

Anderson[10] assume that the resistivity of iron (1) is constant along the melting line at $13.5 \times 10^{-5}\,\Omega$ cm and (2) is a linear function of temperature at constant pressure. In Extended Data Table 1a the temperature T_c at the core density corresponding to (P, T_m) is derived from the equation of state in ref. 31 (see Extended Data Fig. 1). The resistivities at the core density are given by $\rho_c = \rho_m T_c/T_m$, where ρ_m is the melting resistivity. We also tested the effectiveness of Stacey and Anderson's systematics[10] using our resistivity data at the atomic volume of 45 atomic units and temperature 6,000 K. The derived melting resistivity is always close to $13.5 \times 10^{-5}\,\Omega$ cm. Interestingly, our calculations support the systematics of Stacey and Anderson[10], in spite of the importance we find of electron–electron scattering, and their assumption that electron–phonon scattering would give scaling with the melting curve.

The shock compression experiment extrapolation point in Fig. 1 is derived from the formula:

$$\rho(T) = 1.58 + 2.59 \times 10^{-3} T \quad (4)$$

which is the best linear fit of resistivity data from previous shock experiments by Keeler *et al.*[15,16] and Bi *et al.*[17]. $\rho(T)$ is in units of $10^{-5}\,\Omega$ cm. The pressure and temperature of this point come from the Hugoniot line at Earth's core density, as given in Extended Data Fig. 1.

33. Kotliar, G. *et al.* Electronic structure calculations with dynamical mean-field theory. *Rev. Mod. Phys.* **78,** 865 (2006).
34. Georges, A., Kotliar, G., Krauth, W. & Rozenberg, M. J. Dynamical mean-field theory of strongly correlated fermion systems and the limit of infinite dimensions. *Rev. Mod. Phys.* **68,** 13 (1996).
35. Anisimov, V. I., Aryasetiawan, F. & Lichtenstein, A. I. First-principles calculations of the electronic structure and spectra of strongly correlated systems: the LDA+U method. *J. Phys. Condens. Matter* **9,** 767–808 (1997).
36. Czyżyk, M. T. & Sawatzky, G. A. Local-density functional and on-site correlations: The electronic structure of La_2CuO_4 and $LaCuO_3$. *Phys. Rev. B* **49,** 14211 (1994).
37. Werner, P., Comanac, A., de'Medici, L., Troyer, M. & Millis, A. J. Continuous-time solver for quantum impurity models. *Phys. Rev. Lett.* **97,** 076405 (2006).
38. Haule, K. Quantum Monte Carlo impurity solver for cluster dynamical mean-field theory and electronic structure calculations with adjustable cluster base. *Phys. Rev. B* **75,** 155113 (2007).
39. Blaha, P., Schwarz, K., Madsen, G. K. H., Kvasnicka, K. & Luitz, J. in *Wien2K* (ed. Schwarz, K.) (Technische Universitat Wien, 2001).
40. Wu, Z. & Cohen, R. E. More accurate generalized gradient approximation for solids. *Phys. Rev. B* **73,** 235116 (2006).
41. Blöchl, P. E., Jepsen, O. & Andersen, O. K. Improved tetrahedron method for Brillouin-zone integrations. *Phys. Rev. B* **49,** 16223 (1994).
42. Sha, X. & Cohen, R. E. Elastic isotropy of ε-Fe under Earth's core conditions. *Geophys. Res. Lett.* **37,** L10302 (2010).
43. Dziewonski, A. M. & Anderson, D. L. Preliminary reference Earth model. *Phys. Earth Planet. Inter.* **25,** 297–356 (1981).
44. Sha, X. & Cohen, R. E. Thermal effects on lattice strain in ε-Fe under pressure. *Phys. Rev. B* **74,** 064103 (2006).
45. Basov, D. N., Averitt, R. D., van der Marel, D., Dressel, M. & Haule, K. Electrodynamics of correlated electron materials. *Rev. Mod. Phys.* **83,** 471–541 (2011).
46. Cohen, R. E., Fei, Y., Downs, R., Mazin, I. I. & Isaak, D. G. in *High-Pressure Materials Research Materials Research Society Proceedings* (eds Wentzcovitch, R., Hemley, R. J., Nellis, W. J. & Yu, P.) Vol. 499, 27–37 (Materials Research Society, 1998).
47. Ohta, K. *et al.* Experimental and theoretical evidence for pressure-induced metallization in FeO with the rock-salt type structure. *Phys. Rev. Lett.* **108,** 026403 (2012).
48. Shim, J. H., Haule, K. & Kotliar, G. Fluctuating valence in a correlated solid and the anomalous properties of δ-plutonium. *Nature* **446,** 513–516 (2007).
49. Shim, J. H., Haule, K. & Kotliar, G. Modelling the localized to itinerant electronic transition in the heavy fermion system $CeIrIn_5$. *Science* **318,** 1615–1617 (2007).
50. Liu, M. *et al.* Nature of magnetic excitations in superconducting $BaFe_{1.9}Ni_{0.1}As_2$. *Nature Phys.* **8,** 376 (2012).
51. Jarrell, M. & Gubernatis, J. E. Bayesian inference and the analytic continuation of imaginary time quantum Monte Carlo data. *Phys. Rep.* **269,** 133–195 (1996).
52. Pourovskii, L. V. *et al.* Electronic properties and magnetism of iron at the Earth's inner core conditions. *Phys. Rev. B* **87,** 115130 (2013).
53. Khurana, A. Electrical conductivity in the infinite-dimensional Hubbard model. *Phys. Rev. Lett.* **64,** 1990 (1990).
54. Yoo, C. S., Akella, J., Campbell, A. J., Mao, H. K. & Hemley, R. J. Phase diagram of iron by in situ X-ray diffraction: implications for Earth's core. *Science* **270,** 1473–1475 (1995).
55. Brown, J. M. & McQueen, R. G. Phase transitions, Grüneisen parameter, and elasticity for shocked iron between 77 GPa and 400 GPa. *J. Geophys. Res.* **91,** 7485–7494 (1986).
56. Nguyen, J. H. & Holmes, N. C. Melting of iron at the physical conditions of the Earth's core. *Nature* **427,** 339–342 (2004).

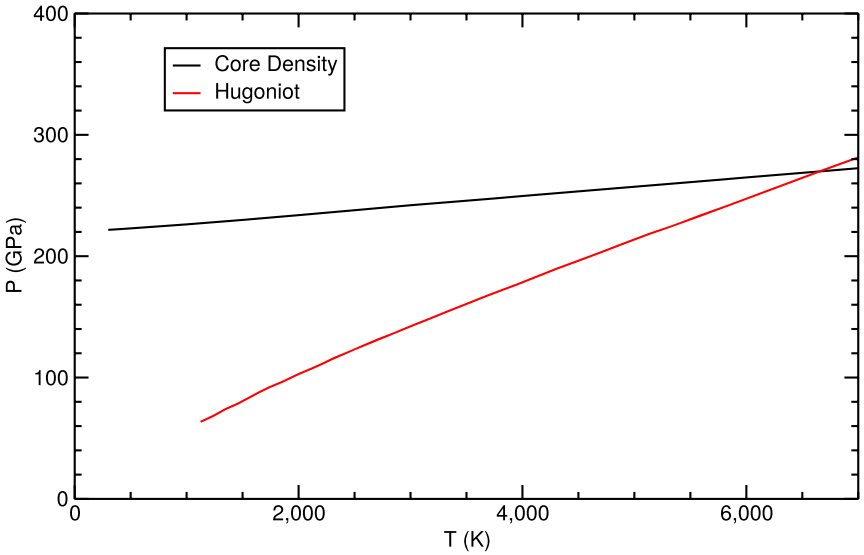

Extended Data Figure 1 | Pressure versus temperature relationship of hcp iron at Earth's core density and along the Hugoniot line[31]. The two lines cross at $P = 269.9$ GPa, $T = 6{,}658$ K at Earth's core density.

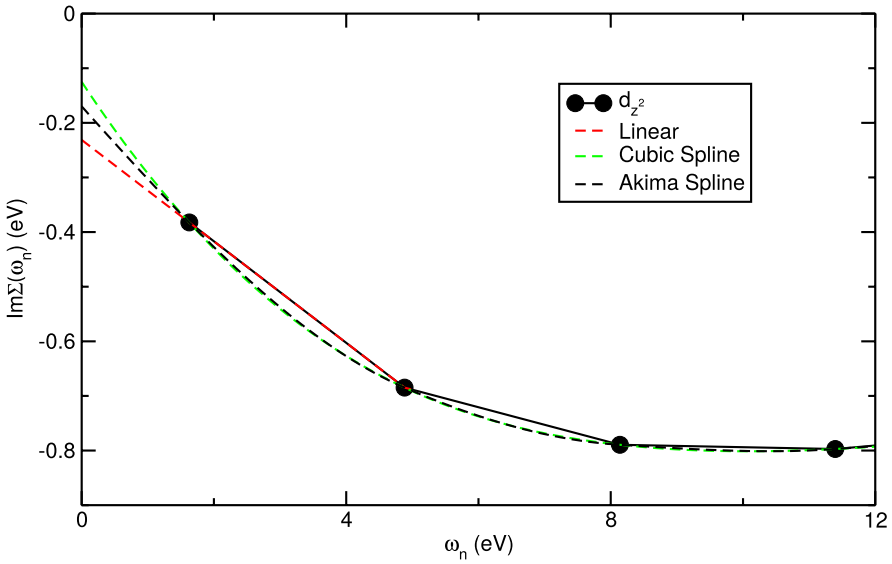

Extended Data Figure 2 | Extrapolation of Im$\Sigma(i\omega_n)$ to zero imaginary frequency. The self-energy is from the d_{z^2} orbital of hcp iron at Earth's core density and 6,000 K. Three extrapolation methods are used: linear, cubic spline and Akima spline. The imaginary part of self-energy at $i0^+$ ranges from -0.23 eV to -0.12 eV.

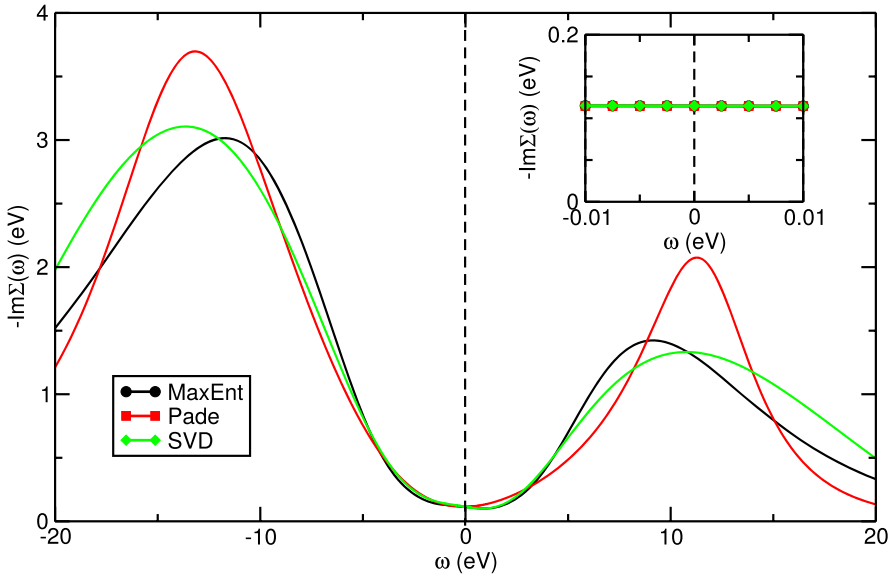

Extended Data Figure 3 | The imaginary part of self-energies in real frequency on the d_{z^2} orbital of hcp iron at Earth's core density and 6,000 K. The self-energies are from three analytic continuation methods: MaxEnt, Padé and singular value decomposition. The inset shows the same imaginary part of self-energies in energy range [−0.01 eV, 0.01 eV] around the Fermi level. The self-energies from three analytic continuation methods agree at the low-energy region.

Extended Data Table 1 | Resistivities from extrapolations and previous experiments

a

P (GPa)	T_m (K)	T_c (K)	ρ (10^{-5} Ω cm)
235	5495	2148	5.28
243	5572	3141	7.61
260	5737	5361	12.62

b

V ($bohr^3$/atom)	P (GPa)	T (K)	ρ (10^{-5} Ω cm)	$\pm$ (10^{-5} Ω cm)
47.8	269.9	6658	18.83	3.07

c

Source	V ($bohr^3$/atom)	P (GPa)	T (K)	ρ (10^{-5} Ω cm)
de Koker et al.	47.8	264.9	6000	6.56
Pozzo et al.	47.8	264	5865	6.65

d

V ($bohr^3$/atom)	P (GPa)	T (K)	ρ (10^{-5} Ω cm)	$\pm$ (10^{-5} Ω cm)
74.2	17	303	2.78	0.31
67.0	37	585	3.19	0.31
63.0	44.4	728	3.59	0.24
61.7	64.3	1240	3.95	0.28
57.2	110	2180	5.35	0.45
55.4	140	2950	6.41	0.42

e

V ($bohr^3$/atom)	P (GPa)	T (K)	ρ (10^{-5} Ω cm)
57.9	101.1	2010	6.9
55.1	146.7	3360	15.2
52.3	208.0	5220	13.1

a, The extrapolated resistivities in Fig. 1 at Earth's core density using the systematics of ref. 10. **b**, The extrapolated resistivity in Fig. 1 at Earth's core density on the Hugoniot. **c**, The resistivities from DFT + MD calculations in Fig. 1 at Earth's core density, extracted from refs 2 and 3. **d**, The atomic volumes, pressures, temperatures and resistivities from shock compression experiments[15,16] in Fig. 2a. **e**, The atomic volumes, pressures, temperatures and resistivities from shock compression experiments by ref. 17 in Fig. 2a.

Extended Data Table 2 | The atomic volumes, pressures, temperatures and resistivities from our study in Fig. 1 and Fig. 2

a

V ($bohr^3$/atom)	P (GPa)	T (K)	ρ_{ep} (10^{-5} Ω cm)	ρ_{ee} (10^{-5} Ω cm)	$\pm\rho_{ee}$ (10^{-6} Ω cm)	$\rho_{ep}+\rho_{ee}$ (10^{-5} Ω cm)
47.8	221.7	300	0.30	0.012	0.0025	0.312
47.8	226.3	1000	1.39	0.14	0.028	1.53
47.8	233.9	2000	2.94	0.55	0.10	3.49
47.8	249.6	4000	6.05	2.68	0.48	8.73
47.8	264.9	6000	9.15	4.75	0.81	13.90
47.8	269.9	6658	10.18	5.48	1.10	15.66
47.8	272.6	7000	10.71	5.87	1.17	16.58

b

V ($bohr^3$/atom)	P (GPa)	T (K)	ρ_{ep} (10^{-5} Ω cm)	ρ_{ee} (10^{-5} Ω cm)	$\pm\rho_{ee}$ (10^{-6} Ω cm)	$\rho_{ep}+\rho_{ee}$ (10^{-5} Ω cm)
63	44.4	728	2.77	0.38	0.057	3.15
57.9	101	2010	5.65	1.65	0.31	7.30
55.1	146.7	3360	6.98	3.28	0.66	10.26
52.3	208	5220	8.84	4.85	0.87	13.69

c

V ($bohr^3$/atom)	P (GPa)	T (K)	ρ_{ep} (10^{-5} Ω cm)	ρ_{ee} (10^{-5} Ω cm)	$\pm\rho_{ee}$ (10^{-6} Ω cm)	$\rho_{ep}+\rho_{ee}$ (10^{-5} Ω cm)
63	28.3	300	0.82	0.063	0.011	0.883
60	50.8	300	0.54	0.042	0.0076	0.582
56.5	84.1	300	0.39	0.024	0.0043	0.414
55	100.0	300	0.37	0.021	0.0040	0.391
58	65	383	0.59	0.054	0.011	0.644

a, DFT+DMFT calculated resistivities in Fig. 1 at Earth's core density. **b**, DFT + DMFT calculated resistivities in Fig. 2a, along the Hugoniot line. **c**, DFT + DMFT calculated resistivities in Fig. 2b, compared with DAC experimental results. ρ_{ep} is the DFPT-calculated resistivity by ref. 1. ρ_{ee} is the resistivity from our DFT + DMFT study.